

# Sliced Wasserstein Kernel for Persistence Diagrams

Mathieu Carrière, Marco Cuturi, Steve Oudot

## Abstract

Persistence diagrams (PDs) play a key role in topological data analysis (TDA), in which they are routinely used to describe topological properties of complicated shapes. PDs enjoy strong stability properties and have proven their utility in various learning contexts. They do not, however, live in a space naturally endowed with a Hilbert structure and are usually compared with non-Hilbertian distances, such as the bottleneck distance. To incorporate PDs in a convex learning pipeline, several kernels have been proposed with a strong emphasis on the stability of the resulting RKHS distance w.r.t. perturbations of the PDs. In this article, we use the Sliced Wasserstein approximation of the Wasserstein distance to define a new kernel for PDs, which is not only provably stable but also discriminative (with a bound depending on the number of points in the PDs) w.r.t. the first diagram distance between PDs. We also demonstrate its practicality, by developing an approximation technique to reduce kernel computation time, and show that our proposal compares favorably to existing kernels for PDs on several benchmarks.

## 1 Introduction

Topological Data Analysis (TDA) is an emerging trend in data science, grounded on topological methods to design descriptors for complex data—see e.g. [5] for an introduction to the subject. The descriptors of TDA can be used in various contexts, in particular statistical learning and geometric inference, where they provide useful insight into the structure of data. Applications of TDA can be found in a number of scientific areas, including computer vision [22], materials science [18], and brain science [32], to name a few. The tools developed in TDA are built upon persistent homology theory [15, 25], and their main output is a descriptor called *persistence diagram* (PD), which encodes the topology of a space at all scales in the form of a point cloud with multiplicities in the plane  $\mathbb{R}^2$ —see Section 2.1 for more details.

**PDs as features.** The main strength of PDs is their stability with respect to perturbations of the data [9, 11]. On the downside, their use in learning tasks is not straightforward. Indeed, a large class of learning methods, such as SVM or PCA, requires a Hilbert structure on the descriptors space, which is not the case for the space of PDs. Actually, many simple operators of  $\mathbb{R}^n$ , such as addition, average or scalar product, have no analogues in that space. Mapping PDs to vectors in  $\mathbb{R}^n$  or in some infinite-dimensional Hilbert space is one possible approach to facilitate their use in discriminative settings.

**Related work.** A series of recent contributions have proposed kernels for PDs, falling into two classes. The first class of methods builds explicit feature maps: One can, for instance, compute and sample functions extracted from PDs [4, 1, 30]; sort the entries of the distance matrices of

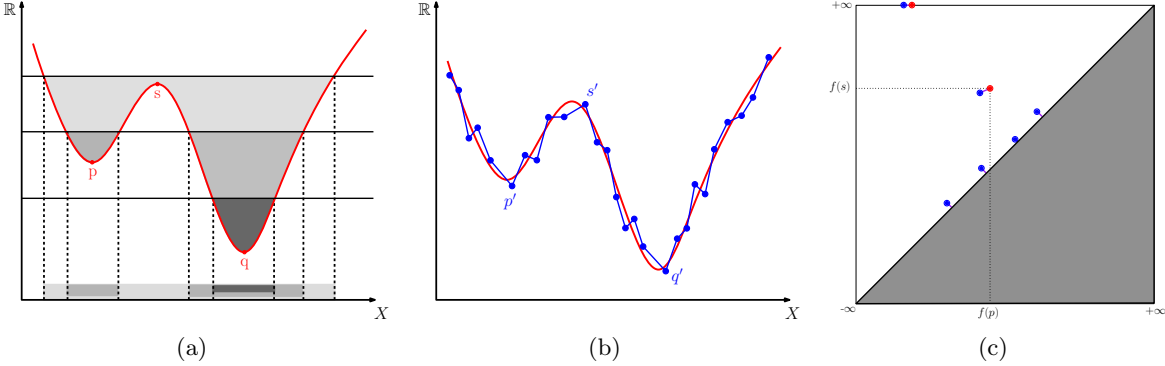


Figure 1: Sketch of persistent homology: (a) the horizontal lines are the boundaries of sublevel sets  $f((-\infty, t])$ , which are colored in decreasing shades of grey. The vertical dotted lines are the boundaries of their different connected components. For instance, a new connected component is created in the sublevel set  $f^{-1}((-\infty, t])$  when  $t = f(p)$ , and it is merged (destroyed) when  $t = f(s)$ ; its lifespan is represented by a copy of the point with coordinates  $(f(p), f(s))$  in the persistence diagram of  $f$  (Figure (c)); (b) a piecewise-linear approximation  $g$  (blue) of the function  $f$  (red) from sampled values; (c) superposition of  $D(f)$  (red) and  $D(g)$  (blue), showing the partial matching of minimum cost (magenta) between the two persistence diagrams.

the PDs [6]; treat the PD points as roots of a complex polynomial, whose coefficients are concatenated [14]. The second class of methods, which is more relevant to our work, defines implicitly feature maps by focusing instead on building kernels for PDs. For instance, [29] use solutions of the heat differential equation in the plane and compare them with the usual  $L^2(\mathbb{R}^2)$  dot product. [19] handle a PD as a discrete measure on the plane, and follow by using kernel mean embeddings with Gaussian kernels—see Section 4 for precise definitions. Both kernels are provably *stable*, in the sense that the metric they induce in their respective reproducing kernel Hilbert space (RKHS) is bounded above by the distance between PDs. Although these kernels are injective, there is no evidence that their induced RKHS distances are discriminative and therefore follow the geometry of the bottleneck distances, which are more widely accepted distances to compare PDs.

**Contributions.** In this article, we use the sliced Wasserstein (SW) distance [26] to define a new kernel for PDs, which we prove to be both stable and discriminative. Specifically, we provide distortion bounds on the SW distance that quantify its ability to mimic bottleneck distances between PDs. This is in contrast to other kernels for PDs, which only focus on stability. We also propose a simple approximation algorithm to speed up the computation of that kernel, confirm experimentally its discriminative power and show that it outperforms experimentally both proposals of [19] and [29] in several supervised classification problems.

## 2 Background

### 2.1 Persistent Homology

Persistent homology is a technique inherited from algebraic topology for computing stable signatures on real-valued functions. Given  $f : X \rightarrow \mathbb{R}$  as input, persistent homology outputs a planar point

set with multiplicities, called the *persistence diagram* of  $f$  and denoted by  $D(f)$ . See Figure 1 for an example. To understand the meaning of each point in this diagram, it suffices to know that, to compute  $D(f)$ , persistent homology considers the family of *sublevel sets* of  $f$ , i.e. the sets of the form  $f^{-1}((-\infty, t])$  for  $t \in \mathbb{R}$ , and it records the *topological events* (e.g. creation or merge of a connected component, creation or filling of a loop, void, etc.) that occur in  $f^{-1}((-\infty, t])$  as  $t$  ranges from  $-\infty$  to  $+\infty$ . Then, each point  $p \in D(f)$  represents the lifespan of a particular *topological feature* (connected component, loop, void, etc.), with its creation and destruction times as coordinates. See again Figure 1 for an illustration.

For the interested reader, we point out that the mathematical tool used by persistent homology to track the topological events in the family of sublevel sets is *homological algebra*, which turns the parametrized family of sublevel sets into a parametrized family of vector spaces and linear maps. Computing persistent homology then boils down to computing a family of bases for the vector spaces, which are compatible with the linear maps. It will be no surprise to the reader familiar with matrix reduction techniques that the simplest way to implement the compatible basis computation is using Gaussian elimination.

**Distance between PDs.** We now define the  *$p$ th diagram distance* between PDs. Let  $p \in \mathbb{N}$  and  $D_1, D_2$  be two PDs. Let  $\Gamma : D_1 \supseteq A \rightarrow B \subseteq D_2$  be a *partial bijection* between  $D_1$  and  $D_2$ . Then, for any point  $x \in A$ , the *cost* of  $x$  is defined as  $c(x) := \|x - \Gamma(x)\|_\infty^p$ , and for any point  $y \in (D_1 \sqcup D_2) \setminus (A \sqcup B)$ , the *cost* of  $y$  is defined as  $c'(y) := \|y - \pi_\Delta(y)\|_\infty^p$ , where  $\pi_\Delta$  is the projection onto the diagonal  $\Delta = \{(x, x) \mid x \in \mathbb{R}\}$ . The cost  $c(\Gamma)$  is defined as:  $c(\Gamma) := (\sum_x c(x) + \sum_y c'(y))^{1/p}$ . We then define the  *$p$ th diagram distance*  $d_p$  as the cost of the best partial bijection:

$$d_p(D_1, D_2) = \inf_{\Gamma} c(\Gamma).$$

In the particular case  $p = +\infty$ , the cost of  $\Gamma$  is defined as  $c(\Gamma) := \max\{\max_x \delta(x) + \max_y \delta'(y)\}$ . The corresponding distance  $d_\infty$  is often called the *bottleneck distance*. One can show that  $d_p \rightarrow d_\infty$  when  $p \rightarrow +\infty$ . A fundamental property of PDs is their stability with respect to (small) perturbations of their originating functions. Indeed, the *stability theorem* [2, 8, 10, 13] asserts that for any  $f, g : X \rightarrow \mathbb{R}$ , we have

$$d_\infty(D(f), D(g)) \leq \|f - g\|_\infty, \quad (1)$$

In practice, persistence diagrams can be used as descriptors for data via the choice of appropriate filtering functions  $f$ , e.g. distance to the data in the ambient space, eccentricity, curvature, etc. The main strengths of the obtained descriptors are: (a) to be provably stable as mentioned previously; (b) to be invariant under reparametrization of the data; and (c) to encode information about the topology of the data, which is complementary and of an essentially different nature compared to geometric or statistical quantities. These properties have made persistence diagrams useful in a variety of contexts, including the ones mentioned in the introduction of the paper. For further details on persistent homology and on applications of persistence diagrams, the interested reader can refer e.g. to [25] and the references therein.

## 2.2 Kernel Methods

**Positive Definite Kernels.** Given a set  $X$ , a function  $k : X \times X \rightarrow \mathbb{R}$  is called a *positive definite kernel* if for all integers  $n$ , for all families  $x_1, \dots, x_n$  of points in  $X$ , the matrix  $[k(x_i, x_j)]_{i,j}$  is itself positive semi-definite. For brevity we will refer to positive definite kernels as kernels in the rest

of the paper. It is known that kernels generalize scalar products, in the sense that, given a kernel  $k$ , there exists a Reproducing Kernel Hilbert Space (RKHS)  $\mathcal{H}_k$  and a *feature map*  $\phi : X \rightarrow \mathcal{H}_k$  such that  $k(x_1, x_2) = \langle \phi(x_1), \phi(x_2) \rangle_{\mathcal{H}_k}$ . A kernel  $k$  also induces a distance  $d_k$  on  $X$  that can be computed as the Hilbert norm of the difference between two embeddings:

$$d_k^2(x_1, x_2) \stackrel{\text{def.}}{=} k(x_1, x_1) + k(x_2, x_2) - 2k(x_1, x_2).$$

We will be particularly interested in this distance, since one of the goals we will aim for will be that of designing a kernel  $k$  for PDs such that  $d_k$  has low distortion with respect to  $d_1$ .

**Negative Definite and RBF Kernels.** A standard way to construct a kernel is to exponentiate the negative of a Euclidean distance. Indeed, the Gaussian kernel for vectors with parameter  $\sigma > 0$  does follow that template approach:  $k_\sigma(x, y) = \exp\left(-\frac{\|x-y\|^2}{2\sigma^2}\right)$ . An important theorem of [3] (Theorem 3.2.2, p.74) states that such an approach to build kernels, namely setting

$$k_\sigma(x, y) \stackrel{\text{def.}}{=} \exp\left(-\frac{f(x, y)}{2\sigma^2}\right),$$

for an arbitrary function  $f$  can only yield a valid positive definite kernel for all  $\sigma > 0$  if and only if  $f$  is a *negative semi-definite* function, namely that, for all integers  $n$ ,  $\forall x_1, \dots, x_n \in X$ ,  $\forall a_1, \dots, a_n \in \mathbb{R}^n$  such that  $\sum_i a_i = 0$ ,  $\sum_{i,j} a_i a_j f(x_i, x_j) \leq 0$ .

Unfortunately, as observed in Appendix A of [28],  $d_1$  is not negative semi-definite (it only suffices to sample a family of point clouds to observe experimentally that more often than not the inequality above will be violated for a particular weight vector  $a$ ). In this article, we use an approximation of  $d_1$  with the *Sliced Wasserstein distance*, which is provably negative semi-definite, and we use it to define a RBF kernel that can be easily tuned thanks to its bandwidth parameter  $\sigma$ .

### 2.3 Wasserstein distance for unnormalized measures on $\mathbb{R}$

The Wasserstein distance [34, §6] is a distance between probability measures. For reasons that will become clear in the next section, we will focus on a variant of that distance: the 1-Wasserstein distance for *nonnegative*, not necessarily normalized, measures on the real line [31, §2]. Let  $\mu$  and  $\nu$  be two nonnegative measures on the real line such that  $|\mu| = \mu(\mathbb{R})$  and  $|\nu| = \nu(\mathbb{R})$  are equal to the same number  $r$ . We define the three following objects:

$$\mathcal{W}(\mu, \nu) = \inf_{P \in \Pi(\mu, \nu)} \iint_{\mathbb{R} \times \mathbb{R}} |x - y| P(dx, dy) \quad (2)$$

$$\mathcal{Q}_r(\mu, \nu) = r \int_{\mathbb{R}} |M^{-1}(x) - N^{-1}(x)| dx \quad (3)$$

$$\mathcal{L}(\mu, \nu) = \inf_{f \in 1\text{-Lipschitz}} \int_{\mathbb{R}} f(x) [\mu(dx) - \nu(dx)] \quad (4)$$

where  $\Pi(\mu, \nu)$  is the set of measures on  $\mathbb{R}^2$  with marginals  $\mu$  and  $\nu$ , and  $M^{-1}$  and  $N^{-1}$  the generalized quantile functions of the probability measures  $\mu/r$  and  $\nu/r$  respectively.

**Proposition 2.1.** *We have  $\mathcal{W} = \mathcal{Q}_r = \mathcal{L}$ . Additionally (i)  $\mathcal{Q}_r$  is negative definite on the space of measures of mass  $r$ ; (ii) for any three positive measures  $\mu, \nu, \gamma$  such that  $|\mu| = |\nu|$ , we have  $\mathcal{L}(\mu + \gamma, \nu + \gamma) = \mathcal{L}(\mu, \nu)$ .*

Equation (2) is the generic Kantorovich formulation of optimal transport, which is easily generalized to other cost functions and spaces, the variant being that we consider an unnormalized mass by reflecting it directly in the set  $\Pi$ . The equality between (2) and (3) is only valid for probability measures on the real line. Because the cost function  $|\cdot|$  is homogeneous, we see that the scaling factor  $r$  can be removed when considering the quantile function and multiplied back. The equality between (2) and (4) is due to the well known Kantorovich duality for a distance cost [34, Particular case 5.4] which can also be trivially generalized to unnormalized measures, proving therefore the main statement of the proposition. The definition of  $Q_r$  shows that the Wasserstein distance is the  $l_1$  norm of  $rM^{-1} - rN^{-1}$ , and is therefore a negative definite kernel (as the  $l_1$  distance between two direct representations of  $\mu$  and  $\nu$  as functions  $rM^{-1}$  and  $rN^{-1}$ ), proving point (i). The second statement is immediate.

We conclude with an important practical remark: for two unnormalized uniform empirical measures  $\mu = \sum_{i=1}^n \delta_{x_i}$  and  $\nu = \sum_{i=1}^n \delta_{y_i}$  of the same size, with ordered  $x_1 \leq \dots \leq x_n$  and  $y_1 \leq \dots \leq y_n$ , one has:  $\mathcal{L}(\mu, \nu) = \sum_{i=1}^n |x_i - y_i| = \|X - Y\|_1$ , where  $X = (x_1, \dots, x_n) \in \mathbb{R}^n$  and  $Y = (y_1, \dots, y_n) \in \mathbb{R}^n$ .

### 3 The Sliced Wasserstein Kernel

#### 3.1 The Sliced Wasserstein Kernel

In this section we define a new kernel between PDs, called the *Sliced Wasserstein* (SW) kernel, based on the Sliced Wasserstein metric of [26]. The idea underlying this metric is to slice the plane with lines passing through the origin, to project the measures onto these lines where  $\mathcal{W}$  is computed, and to integrate those distances over all possible lines. Formally:

**Definition 3.1.** Given  $\theta \in \mathbb{R}^2$  with  $\|\theta\|_2 = 1$ , let  $L(\theta)$  denote the line  $\{\lambda\theta \mid \lambda \in \mathbb{R}\}$ , and let  $\pi_\theta : \mathbb{R}^2 \rightarrow L(\theta)$  be the orthogonal projection onto  $L(\theta)$ . Let  $D_1, D_2$  be two PDs, and let  $\mu_1^\theta := \sum_{p \in D_1} \delta_{\pi_\theta(p)}$  and  $\mu_{1\Delta}^\theta := \sum_{p \in D_1} \delta_{\pi_\theta \circ \pi_\Delta(p)}$ , and similarly for  $\mu_2^\theta$ , where  $\pi_\Delta$  is the orthogonal projection onto the diagonal. Then, the Sliced Wasserstein distance is defined as:

$$\text{SW}(D_1, D_2) \stackrel{\text{def.}}{=} \frac{1}{2\pi} \int_{\mathbb{S}_1} \mathcal{W}(\mu_1^\theta + \mu_{2\Delta}^\theta, \mu_2^\theta + \mu_{1\Delta}^\theta) d\theta.$$

Note that, by symmetry, one can restrict on the half-circle  $[-\frac{\pi}{2}, \frac{\pi}{2}]$  and normalize by  $\pi$  instead of  $2\pi$ . Since  $\mathcal{Q}_r$  is negative semi-definite, we can deduce that SW itself is negative semi-definite:

**Lemma 3.2.** Let  $X$  be the set of bounded, finite PDs. Then, SW is negative semi-definite on  $X$ .

*Proof.* Let  $n \in \mathbb{N}^*$ ,  $a_1, \dots, a_n \in \mathbb{R}$  such that  $\sum_i a_i = 0$  and  $D_1, \dots, D_n \in X$ . Given  $1 \leq i \leq n$ , we let  $\tilde{\mu}_i^\theta := \mu_i^\theta + \sum_{q \in D_k, k \neq i} \delta_{\pi_\theta \circ \pi_\Delta(q)}$ ,  $\tilde{\mu}_{ij\Delta}^\theta := \sum_{p \in D_k, k \neq i, j} \delta_{\pi_\theta \circ \pi_\Delta(p)}$  and  $d = \sum_i |D_i|$ . Then:

$$\begin{aligned} \sum_{i,j} a_i a_j \mathcal{W}(\mu_i^\theta + \mu_{j\Delta}^\theta, \mu_j^\theta + \mu_{i\Delta}^\theta) &= \sum_{i,j} a_i a_j \mathcal{L}(\mu_i^\theta + \mu_{j\Delta}^\theta, \mu_j^\theta + \mu_{i\Delta}^\theta) \\ &= \sum_{i,j} a_i a_j \mathcal{L}(\mu_i^\theta + \mu_{j\Delta}^\theta + \mu_{ij\Delta}^\theta, \mu_j^\theta + \mu_{i\Delta}^\theta + \mu_{ij\Delta}^\theta) \\ &= \sum_{i,j} a_i a_j \mathcal{L}(\tilde{\mu}_i^\theta, \tilde{\mu}_j^\theta) = \sum_{i,j} a_i a_j \mathcal{Q}_d(\tilde{\mu}_i^\theta, \tilde{\mu}_j^\theta) \leq 0 \end{aligned}$$

The result follows by linearity of integration.  $\square$

Hence, the theorem of [3] allows us to define a valid kernel with:

$$k_{\text{SW}}(D_1, D_2) \stackrel{\text{def.}}{=} \exp\left(-\frac{\text{SW}(D_1, D_2)}{2\sigma^2}\right). \quad (5)$$

## 3.2 Metric Equivalence

We now give the main theoretical result of this article, which states that SW is *equivalent* to  $d_1$ . This has to be compared with [29] and [19], which only prove stability and injectivity. Our equivalence result states that  $k_{\text{SW}}$ , in addition to be stable and injective, preserves the metric between PDs, which should intuitively lead to an improvement of the classification power. This intuition is illustrated in Section 4 and Figure 6, where we show an improvement of classification accuracies on several benchmark applications.

### 3.2.1 Stability

**Theorem 3.3.** *Let  $X$  be the set of bounded and finite PDs. Then, SW is stable w.r.t  $d_1$  on  $X$ . For any  $D_1, D_2 \in X$ , one has:*

$$\text{SW}(D_1, D_2) \leq 2\sqrt{2}d_1(D_1, D_2).$$

*Proof.* Let  $\theta \in \mathbb{R}^2$  be such that  $\|\theta\|_2 = 1$ . Let  $D_1, D_2 \in X$ , and let  $D_1^\theta = \{\pi_\theta(p) : p \in D_1\} \cup \{\pi_\theta \circ \pi_\Delta(q) : q \in D_2\}$  and  $D_2^\theta = \{\pi_\theta(q) : q \in D_2\} \cup \{\pi_\theta \circ \pi_\Delta(p) : p \in D_1\}$ . Let  $\gamma^*$  be the one-to-one bijection between  $D_1^\theta$  and  $D_2^\theta$  induced by  $\mathcal{W}(\mu_1^\theta + \mu_{2\Delta}^\theta, \mu_2^\theta + \mu_{1\Delta}^\theta)$ , and let  $\gamma$  be the one-to-one bijection between  $D_1 \cup \pi_\Delta(D_2)$  and  $D_2 \cup \pi_\Delta(D_1)$  induced by the partial bijection achieving  $d_1(D_1, D_2)$ . Then  $\gamma$  naturally induces a one-to-one matching  $\gamma_\theta$  between  $D_1^\theta$  and  $D_2^\theta$  with:

$$\gamma_\theta = \{(\pi_\theta(p), \pi_\theta(q)) : (p, q) \in \gamma\} \cup \{(\pi_\theta \circ \pi_\Delta(p), \pi_\theta \circ \pi_\Delta(q)) : (p, q) \in \gamma, p, q \notin \text{im}(\pi_\Delta)\}.$$

Now, one has the following inequalities:

$$\begin{aligned} \mathcal{W}(\mu_1^\theta + \mu_{2\Delta}^\theta, \mu_2^\theta + \mu_{1\Delta}^\theta) &= \sum_{(x,y) \in \gamma^*} |x - y| \\ &\leq \sum_{(\pi_\theta(p), \pi_\theta(q)) \in \gamma_\theta} |p^T \theta - q^T \theta| \text{ since } \gamma_\theta \text{ is not the optimal matching between } D_i^\theta \text{ and } D_j^\theta \\ &\leq \sum_{(\pi_\theta(p), \pi_\theta(q)) \in \gamma_\theta} \|p - q\|_2 \text{ by the Cauchy-Schwarz inequality since } \|\theta\|_2 = 1 \\ &\leq \sqrt{2} \sum_{(\pi_\theta(p), \pi_\theta(q)) \in \gamma_\theta} \|p - q\|_\infty \text{ since } \|\cdot\|_2 \leq \sqrt{2}\|\cdot\|_\infty \\ &\leq 2\sqrt{2} \sum_{(p,q) \in \gamma} \|p - q\|_\infty \text{ since } \|\pi_\Delta(p) - \pi_\Delta(q)\|_\infty \leq \|p - q\|_\infty \\ &= 2\sqrt{2}d_1(D_1, D_2) \end{aligned}$$

Hence, we have  $\text{SW}(D_1, D_2) \leq 2\sqrt{2}d_1(D_1, D_2)$ .  $\square$

We now prove the discriminativity of SW. For this, we need a stronger assumption on the PDs, namely their cardinalities have not only to be finite, but also bounded by some  $N \in \mathbb{N}^*$ .

### 3.2.2 Discriminativity

**Theorem 3.4.** *Let  $X$  be the set of bounded PDs with cardinalities bounded by  $N \in \mathbb{N}^*$ . Then, SW is discriminative w.r.t.  $d_1$  on  $X$ . For any  $D_1, D_2 \in X$ , one has:*

$$\frac{1}{2M} d_1(D_1, D_2) \leq \text{SW}(D_1, D_2),$$

where  $M = 1 + 2N(2N - 1)$ .

*Proof.* Let  $D_1, D_2 \in X$ . Let  $\mathbb{S}_1^+ \subseteq \mathbb{S}_1$  be the subset of the circle delimited by the angles  $[-\frac{\pi}{2}, \frac{\pi}{2}]$ . Let us consider the following set:

$$\Theta_1 = \{\theta \in \mathbb{S}_1^+ \mid \exists p_1, p_2 \in D_1 : \theta^T(p_2 - p_1) = 0\},$$

and similarly:

$$\Theta_2 = \{\theta \in \mathbb{S}_1^+ \mid \exists q_1, q_2 \in D_2 : \theta^T(q_2 - q_1) = 0\}.$$

Now, we let  $\Theta = \Theta_1 \cup \Theta_2 \cup \{-\frac{\pi}{2}, \frac{\pi}{2}\}$  be the union of these sets, and sort  $\Theta$  in decreasing order. One has  $|\Theta| \leq 2N(2N - 1) + 2 = M + 1$  since a vector  $\theta$  that is orthogonal to a line defined by a specific pair of points  $(p_1, p_2)$  appears exactly once in  $\mathbb{S}_1^+$ .

For any  $\theta$  that is between two consecutive  $\theta_k, \theta_{k+1} \in \Theta$ , the order of the projections onto  $L(\theta)$  of the points of both  $D_1$  and  $D_2$  remains the same. Given any point  $p \in D_1 \cup \pi_\Delta(D_2)$ , we let  $\gamma(p) \in D_2 \cup \pi_\Delta(D_1)$  be its matching point according to the matching given by  $\mathcal{W}(\mu_1^\theta + \mu_{2\Delta}^\theta, \mu_2^\theta + \mu_{1\Delta}^\theta)$ . Then, one has the following equalities:

$$\begin{aligned} & \int_{\theta_k}^{\theta_{k+1}} \mathcal{W}(\mu_1^\theta + \mu_{2\Delta}^\theta, \mu_2^\theta + \mu_{1\Delta}^\theta) \, d\theta \\ &= \int_{\theta_k}^{\theta_{k+1}} \sum_{p \in D_1 \cup \pi_\Delta(D_2)} |(p - \gamma(p))^T \theta| \, d\theta \\ &= \sum_{p \in D_1 \cup \pi_\Delta(D_2)} \|p - \gamma(p)\|_2 \int_0^{\theta_{k+1} - \theta_k} |\cos(\alpha_p + \beta)| \, d\beta \text{ where } \alpha_p = \angle(p - \gamma(p), \theta_k) \end{aligned}$$

We need to lower bound  $\int_0^{\theta_{k+1} - \theta_k} |\cos(\alpha_p + \beta)| \, d\beta$ . Since  $\theta_{k+1} - \theta_k \leq \pi$ , one can show that this integral cannot be less than  $\frac{(\theta_{k+1} - \theta_k)^2}{2\pi}$  using cosine concavity—see Figure 2. Hence, we now have the following lower bound:

$$\begin{aligned} & \int_{\theta_k}^{\theta_{k+1}} \mathcal{W}(\mu_1^\theta + \mu_{2\Delta}^\theta, \mu_2^\theta + \mu_{1\Delta}^\theta) \, d\theta \geq \frac{(\theta_{k+1} - \theta_k)^2}{2\pi} \sum_{p \in D_1 \cup \pi_\Delta(D_2)} \|p - \gamma(p)\|_2 \\ & \geq \frac{(\theta_{k+1} - \theta_k)^2}{2\pi} \sum_{p \in D_1 \cup \pi_\Delta(D_2)} \|p - \gamma(p)\|_\infty \geq \frac{(\theta_{k+1} - \theta_k)^2}{2\pi} \sum_{\substack{p \notin \pi_\Delta(D_2) \\ \text{or } \gamma(p) \notin \pi_\Delta(D_1)}} \|p - \gamma(p)\|_\infty \\ & \geq \frac{(\theta_{k+1} - \theta_k)^2}{2\pi} d_1(D_1, D_2). \end{aligned}$$

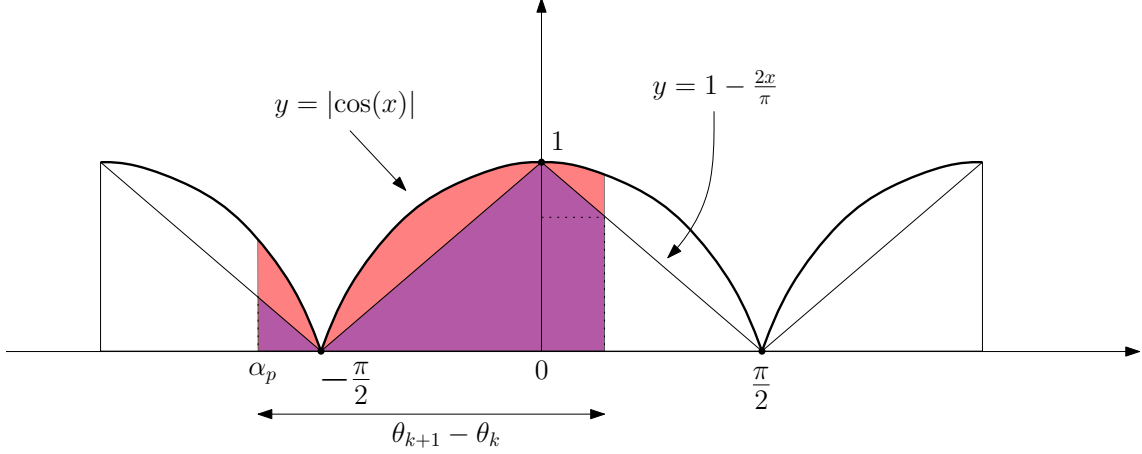


Figure 2: The integral of  $|\cos(\cdot)|$  has a lower bound that depends on the length of the integral support. In particular, when  $\theta_{k+1} - \theta_k \leq \pi$ , this integral is more than  $\frac{(\theta_{k+1} - \theta_k)^2}{2\pi}$  by the Cauchy-Schwarz inequality.

Let  $\Theta = \{\theta_1 = -\frac{\pi}{2}, \theta_2, \dots, \theta_{|\Theta|} = \frac{\pi}{2}\}$ . Then, one has:

$$\begin{aligned}
\text{SW}(D_1, D_2) &= \frac{1}{\pi} \int_{-\frac{\pi}{2}}^{\frac{\pi}{2}} \mathcal{W}(\mu_1^\theta + \mu_{2\Delta}^\theta, \mu_2^\theta + \mu_{1\Delta}^\theta) d\theta \\
&= \frac{1}{\pi} \sum_{k=1}^{|\Theta|-1} \int_{\theta_k}^{\theta_{k+1}} \mathcal{W}(\mu_1^\theta + \mu_{2\Delta}^\theta, \mu_2^\theta + \mu_{1\Delta}^\theta) d\theta \\
&\geq \left( \sum_{k=1}^{|\Theta|-1} (\theta_{k+1} - \theta_k)^2 \right) \frac{d_1(D_1, D_2)}{2\pi^2} \\
&\geq \frac{\pi^2}{|\Theta| - 1} \frac{d_1(D_1, D_2)}{2\pi^2} \text{ by the Cauchy-Schwarz inequality} \\
&\geq \frac{d_1(D_1, D_2)}{2M}
\end{aligned}$$

Hence, SW is discriminative.  $\square$

In particular, Theorems 3.3 and 3.4 allow us to show that  $d_{\text{SW}}$ , the distance induced by  $k_{\text{SW}}$  in its RKHS, is also equivalent to  $d_1$  in a broader sense: there exist continuous, positive and monotone functions  $g, h$  such that  $g(0) = h(0) = 0$  and  $h \circ d_1 \leq d_{\text{SW}} \leq g \circ d_1$ .

The condition on the cardinalities of PDs can be relaxed. Indeed, one can prove that the feature map  $\phi_{\text{SW}}$  induced by  $k_{\text{SW}}$  is injective when the PDs are only assumed to be finite and bounded:

**Proposition 3.5.** *Let  $X$  be the set of bounded and finite PDs. The feature map  $\phi_{\text{SW}}$  associated to  $k_{\text{SW}}$  is continuous and injective w.r.t.  $d_1$  on  $X$ .*

*Proof.* Note that if the PDs have bounded cardinalities, Proposition 3.5 is an immediate consequence of Theorem 3.4. One has that  $\phi_{\text{SW}}$  is continuous since  $d_{\text{SW}}$  is stable (cf Theorem 3.3). Now, let  $D_1, D_2 \in X$  such that  $d_{\text{SW}}(D_1, D_2) = \|\phi_{\text{SW}}(D_1) - \phi_{\text{SW}}(D_2)\| = 0$ . We necessarily have  $\text{SW}(D_1, D_2) = 0$ . Assume that  $d_1(D_1, D_2) > 0$ . Then, there must be a point  $p$  in  $D_1$  that is not in  $D_2$ . The Sliced Wasserstein distance being 0, there must be, for every  $\theta \in \mathbb{S}_1$ , a point  $q_\theta$  in  $D_2$  that has the same projection onto  $L(\theta)$  as  $p$ :  $\pi_\theta(q_\theta) = \pi_\theta(p)$ , i.e.  $q_\theta \in (\pi_\theta(p), p)$ , the line defined by the pair  $\pi_\theta(p), p$ . All these lines  $(\pi_\theta(p), p)$  intersect at  $p \neq q_\theta$ . Thus,  $q_{\theta_1} \neq q_{\theta_2}$  for any  $\theta_1 \neq \theta_2$ , hence  $D_j$  must include an infinite number of points, which is impossible. Thus,  $d_1(D_1, D_2) = 0$  and  $\phi_{\text{SW}}$  is injective.  $\square$

In particular,  $k_{\text{SW}}$  can be turned into a universal kernel by considering  $\exp(k_{\text{SW}})$  (cf Theorem 1 in [21]). This can be useful in a variety of tasks, including tests on distributions of PDs.

### 3.3 Computation

**Approximate computation.** In practice, we propose to approximate  $k_{\text{SW}}$  in  $O(N \log(N))$  time using Algorithm 1. This algorithm first samples  $M$  directions in the half-circle  $\mathbb{S}_1^+$ ; it then computes, for each sample  $\theta_i$  and for each PD  $D$ , the scalar products between the points of  $D$  and  $\theta_i$ , to sort them next in a vector  $V_{\theta_i}(D)$ . Finally, the  $\ell_1$ -norm between the vectors is averaged over the sampled directions:  $\text{SW}_M(D_1, D_2) = \frac{1}{M} \sum_{i=1}^M \|V_{\theta_i}(D_1) - V_{\theta_i}(D_2)\|_1$ . Note that one can easily adapt the proof of Lemma 3.2 to show that  $\text{SW}_M$  is negative semi-definite by using the linearity of the sum. Hence, this approximation remains a kernel. If the two PDs have cardinalities bounded by  $N$ , then the running time of this procedure is  $O(MN \log(N))$ . This approximation of  $k_{\text{SW}}$  is useful since, as shown in Section 4, we have observed empirically that just a few directions are sufficient to get good classification accuracies.

---

**Algorithm 1:** Approximate computation of SW

---

**Input:**  $D_1 = \{p_1^1 \dots p_{N_1}^1\}$ ,  $D_2 = \{p_1^2 \dots p_{N_2}^2\}$ ,  $M$ .  
 Add  $\pi_\Delta(D_1)$  to  $D_2$  and vice-versa.  
 Let  $\text{SW} = 0$ ;  $\theta = -\pi/2$ ;  $s = \pi/M$ ;  
**for**  $i = 1 \dots M$  **do**  
   Store the products  $\langle p_k^1, \theta \rangle$  in an array  $V_1$ ;  
   Store the products  $\langle p_k^2, \theta \rangle$  in an array  $V_2$ ;  
   Sort  $V_1$  and  $V_2$  in ascending order;  
    $\text{SW} = \text{SW} + s \|V_1 - V_2\|_1$ ;  
    $\theta = \theta + s$ ;  
**end for**  
**Output:**  $(1/\pi)\text{SW}$ ;

---

**Exact computation.** A PD is said to be in *general position* if it has no triplet of aligned points. If the PDs have cardinalities bounded by  $N$ , then the exact kernel computation for PDs in general position can be done in  $O(N^2 \log(N))$  time with Algorithm 2. In practice, given  $D_1$  and  $D_2$ , we slightly modify them with infinitesimally small random perturbations. The resulting PDs  $\tilde{D}_1$  and  $\tilde{D}_2$  are in general position and we can approximate  $k_{\text{SW}}(D_1, D_2)$  with  $k_{\text{SW}}(\tilde{D}_1, \tilde{D}_2)$ .

---

**Algorithm 2:** Exact computation of SW

---

**Input:** PD  $D_1 = \{p_1^1 \dots p_{N_1}^1\}$  with  $|D_1| = N_1$ , PD  $D_2 = \{p_1^2 \dots p_{N_2}^2\}$  with  $|D_2| = N_2$

1 Let  $A^1 = \[], A^2 = \[], V_1 = \[], V_2 = \[], B_1 = [\[] \dots \[]], B_2 = [\[] \dots \[]], SW = 0;$

2 **for**  $i = 1 \dots N_1$  **do**

3   | Add  $p_{N_2+i}^2 := \pi_\Delta(p_j^1)$  to  $D_2$ ;

4 **for**  $i = 1 \dots N_2$  **do**

5   | Add  $p_{N_1+i}^1 := \pi_\Delta(p_j^2)$  to  $D_1$ ;

6 **for**  $i = 1, 2$  **do**

7   | **for**  $j = 1 \dots N_1 + N_2 - 1$  **do**

8     |   | **for**  $k = j + 1 \dots N_1 + N_2$  **do**

9       |     | Add  $\angle [p_j^i - p_k^i]^\perp \in [-\frac{\pi}{2}, \frac{\pi}{2}]$  to  $A^i$ ;

10   | Sort  $A^i$  in ascending order;

11   | **for**  $j = 1 \dots N_1 + N_2$  **do**

12     |   | Add  $(p_j^i, -\frac{\pi}{2})$  to  $V_i$ ;

13   | Sort  $V_i$  in ascending order;

14   | Let  $f_i : p_j^i \mapsto$  position of  $(p_j^i, -\frac{\pi}{2})$  in  $V_i$ ;

15   | **for**  $j = 1 \dots (N_1 + N_2)(N_1 + N_2 - 1)/2$  **do**

16     |   | Let  $A_j^i = \angle [p_{k_1}^i - p_{k_2}^i]^\perp$ ;

17     |   | Add  $(p_{k_1}^i, A_j^i)$  to  $B_i[f_i(p_{k_1}^i)]$ ; Add  $(p_{k_2}^i, A_j^i)$  to  $B_i[f_i(p_{k_2}^i)]$ ;

18     |   | Swap  $f_i(p_{k_1}^i)$  and  $f_i(p_{k_2}^i)$ ;

19   | **for**  $j = 1 \dots N_1 + N_2$  **do**

20     |   | Add  $(p_j^i, \frac{\pi}{2})$  to  $B_i[f_i(p_j^i)]$ ;

21 **for**  $i = 1 \dots N_1 + N_2$  **do**

22   | Let  $k_1 = 0, k_2 = 0$ ;

23   | Let  $\theta_m = -\frac{\pi}{2}$  and  $\theta_M = \min\{B_1[i][k_1]_2, B_2[i][k_2]_2\}$ ;

24   | **while**  $\theta_m \neq \frac{\pi}{2}$  **do**

25     |   |  $\theta_m = \theta_M$ ;

26     |   | **if**  $\theta_M == B_1[i][k_1]_2$  **then**  $k_1 = k_1 + 1$ ; **else**  $k_2 = k_2 + 1$ ;

27     |   |  $\theta_M = \min\{B_1[i][k_1]_2, B_2[i][k_2]_2\}$ ;

28     |   |  $SW = SW + \|B_1[i][k_1]_1 - B_2[i][k_2]_1\|_2 \int_0^{\theta_M - \theta_m} \cos(\angle(B_1[i][k_1]_1 - B_2[i][k_2]_1, \theta_m) + \theta) d\theta$

29 **return**  $\frac{1}{\pi}SW$ ;

---

TASK	TRAINING	TEST	LABELS
ORBIT	175	75	5
TEXTURE	240	240	24
HUMAN	415	1618	8
AIRPLANE	300	980	4
ANT	364	1141	5
BIRD	257	832	4
FOURLEG	438	1097	6
OCTOPUS	334	1447	2
FISH	304	905	3

Table 1: Number of instances in the training set, the test set and number of labels.

TASK	$k_{\text{PSS}} (10^{-3})$	$k_{\text{PWG}} (1000)$	$k_{\text{SW}} (6)$
ORBIT	$63.6 \pm 1.2$	$77.7 \pm 1.2$	<b><math>83.7 \pm 0.5</math></b>
TEXTURE	<b><math>98.8 \pm 0.0</math></b>	$95.8 \pm 0.0$	$96.1 \pm 0.4$
TASK	$k_{\text{PSS}}$	$k_{\text{PWG}}$	$k_{\text{SW}}$
HUMAN	$68.5 \pm 2.0$	$64.2 \pm 1.2$	<b><math>74.0 \pm 0.2</math></b>
AIRPLANE	$65.4 \pm 2.4$	$61.3 \pm 2.9$	<b><math>72.6 \pm 0.2</math></b>
ANT	$86.3 \pm 1.0$	$87.4 \pm 0.5$	<b><math>92.3 \pm 0.2</math></b>
BIRD	$67.7 \pm 1.8$	<b><math>72.0 \pm 1.2</math></b>	$67.0 \pm 0.5$
FOURLEG	$67.0 \pm 2.5$	$64.0 \pm 0.6$	<b><math>73.0 \pm 0.4</math></b>
OCTOPUS	$77.6 \pm 1.0$	$78.6 \pm 1.3$	<b><math>85.2 \pm 0.5</math></b>
FISH	$76.1 \pm 1.6$	<b><math>79.8 \pm 0.5</math></b>	$75.0 \pm 0.4$

Table 2: Classification accuracies (%) for the benchmark applications.

## 4 Experiments

In this section, we compare  $k_{\text{SW}}$  to  $k_{\text{PSS}}$  and  $k_{\text{PWG}}$  on several benchmark applications for which PDs have been proven useful. We compare these kernels in terms of classification accuracies and computational cost. We review first our experimental setting, and review these tasks one by one.

**Experimental setting** All kernels are handled with the LIBSVM [7] implementation of  $C$ -SVM, and results are averaged over 10 runs on a 2.4GHz Intel Xeon E5530 Quad Core. The cost factor  $C$  is cross-validated in the following grid:  $\{0.001, 0.01, 0.1, 1, 10, 100, 1000\}$ . Table 1 summarizes the properties of the datasets we consider, namely number of labels, as well as training and test instances for each task. Figure 3 and 4 illustrate how we use PDs to represent complex data. We first describe the two baselines we considered, along with their parameterization, followed by our proposal.

**PSS.** The *Persistence Scale Space* kernel  $k_{\text{PSS}}$  [29] is defined as the scalar product of the two solutions of the heat diffusion equation with initial Dirac sources located at the PD points. It has

TASK	$k_{\text{PSS}} (10^{-3})$	$k_{\text{PWG}} (1000)$	$k_{\text{SW}} (6)$	
ORBIT	$N(124 \pm 8.4)$	$N(144 \pm 14)$	$415 \pm 7.9 + NC$	
TEXTURE	$N(165 \pm 27)$	$N(101 \pm 9.6)$	$482 \pm 68 + NC$	
TASK	$k_{\text{PSS}}$	$k_{\text{PWG}}$	$k_{\text{SW}}$	$k_{\text{SW}} (10)$
HUMAN	$N(29 \pm 0.3)$	$N(318 \pm 22)$	$2270 \pm 336 + NC$	$107 \pm 14 + NC$
AIRPLANE	$N(0.8 \pm 0.03)$	$N(5.6 \pm 0.02)$	$44 \pm 5.4 + NC$	$10 \pm 1.6 + NC$
ANT	$N(1.7 \pm 0.01)$	$N(12 \pm 0.5)$	$92 \pm 2.8 + NC$	$16 \pm 0.4 + NC$
BIRD	$N(0.5 \pm 0.01)$	$N(3.6 \pm 0.02)$	$27 \pm 1.6 + NC$	$6.6 \pm 0.8 + NC$
FOURLEG	$N(10 \pm 0.07)$	$N(113 \pm 13)$	$604 \pm 25 + NC$	$52 \pm 3.2 + NC$
OCTOPUS	$N(1.4 \pm 0.01)$	$N(11 \pm 0.8)$	$75 \pm 1.4 + NC$	$14 \pm 2.1 + NC$
FISH	$N(1.2 \pm 0.004)$	$N(9.6 \pm 0.03)$	$72 \pm 4.8 + NC$	$12 \pm 1.1 + NC$

Table 3: Gram matrices computation time (s) for the benchmark applications. As explained in the text,  $N$  represents the size of the set of possible parameters, and we have  $N = 13$  for  $k_{\text{PSS}}$ ,  $N = 5 \times 5 \times 5 = 125$  for  $k_{\text{PWG}}$  and  $N = 3 \times 5 = 15$  for  $k_{\text{SW}}$ .  $C$  is a constant that depends only on the training size. In all our applications, it is less than 0.1s.

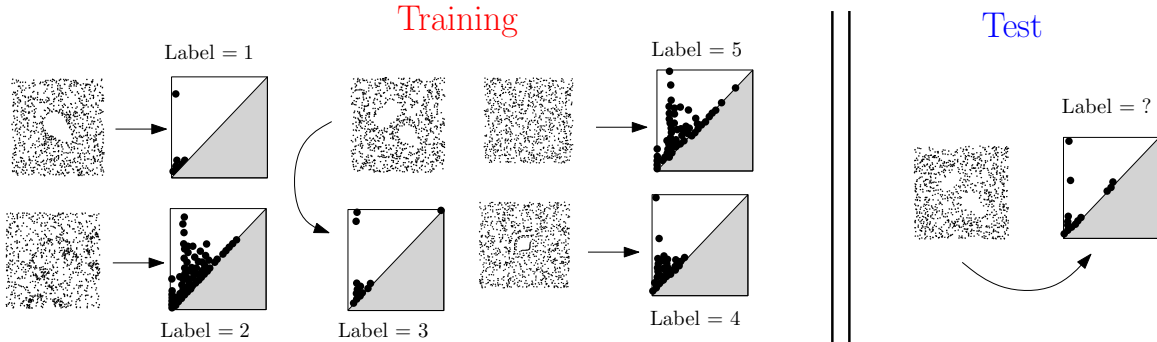


Figure 3: Sketch of the orbit recognition task. Each parameter  $r$  in the 5 possible choices leads to a specific behavior of the orbit. The goal is to recover parameters from the persistent homology of orbits in the test set.

the following closed form expression:

$$k_{\text{PSS}}(D_1, D_2) = \frac{1}{8\pi t} \sum_{p \in D_1} \sum_{q \in D_2} \exp\left(-\frac{\|p - q\|^2}{8t}\right) - \exp\left(-\frac{\|p - \bar{q}\|^2}{8t}\right),$$

where  $\bar{q} = (y, x)$  is the symmetric of  $q = (x, y)$  along the diagonal. Since there is no clear heuristic on how to tune  $t$ , this parameter is chosen in the applications by ten-fold cross-validation with random 50%-50% training-test splits and with the following set of  $N_{\text{PSS}} = 13$  values: 0.001, 0.005, 0.01, 0.05, 0.1, 0.5, 1, 5, 10, 50, 100, 500 and 1000.

**PWG.** Let  $K, p > 0$  and  $D_1$  and  $D_2$  be two PDs. Let  $k_\rho$  be the Gaussian kernel with parameter  $\rho > 0$ . Let  $\mathcal{H}_\rho$  be the RKHS associated to  $k_\rho$ . Let  $\mu_1 := \sum_{x \in D_1} \arctan(K_{\text{pers}}(x)^p) k_\rho(\cdot, x) \in \mathcal{H}_\rho$  be the kernel mean embedding of  $D_1$  weighted by the diagonal distances. Let  $\mu_2$  be defined similarly. Let  $\tau > 0$ . The *Persistence Weighted Gaussian* kernel  $k_{\text{PWG}}$  [19, 20] is defined as the Gaussian

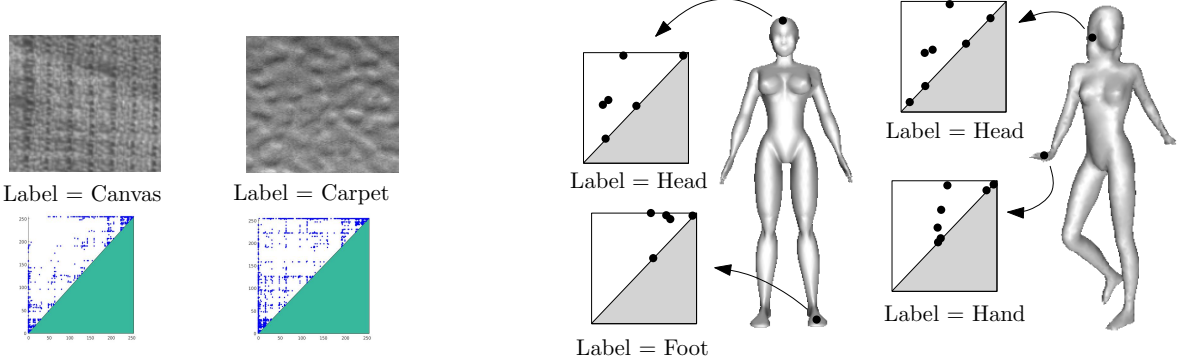


Figure 4: Examples of PDs computed on texture images from the *OUTEX00000* dataset and PDs computed from points on 3D shapes. One can see that corresponding points in different shapes have similar PDs.

kernel with parameter  $\tau$  on  $\mathcal{H}_\rho$ :

$$k_{\text{PWG}}(D_1, D_2) = \exp\left(-\frac{\|\mu_1 - \mu_2\|_{\mathcal{H}_\rho}}{2\tau^2}\right).$$

The authors in [19] provide heuristics to compute  $K$ ,  $\rho$  and  $\tau$  and give a rule of thumb to tune  $p$ . Hence, in the applications we select  $p$  according to the rule of thumb, and we use ten-fold cross-validation with random 50%-50% training-test splits to chose  $K$ ,  $\rho$  and  $\tau$ . The ranges of possible values is obtained by multiplying the values computed with the heuristics with the following range of 5 factors: 0.01, 0.1, 1, 10 and 100, leading to  $N_{\text{PWG}} = 5 \times 5 \times 5 = 125$  different sets of parameters.

**Parameters for  $k_{\text{SW}}$ .** The kernel we propose has only one parameter, the bandwidth  $\sigma$  in Eq. 5, which we choose using ten-fold cross-validation with random 50%-50% training-test splits. The range of possible values is obtained by computing the squareroot of the median, the first and the last deciles of all  $\text{SW}(D_i, D_j)$  in the training set, then by multiplying these values by the following range of 5 factors: 0.01, 0.1, 1, 10 and 100, leading to  $N_{\text{SW}} = 5 \times 3 = 15$  possible values.

**Parameter Tuning.** The bandwidth of  $k_{\text{SW}}$  is, in practice, easier to tune than the parameters of its two competitors when using grid search. Indeed, as is the case for all infinitely divisible kernels, the Gram matrix does not need to be recomputed for each choice of  $\sigma$ , since it only suffices to compute all the Sliced Wasserstein distances between PDs in the training set once. On the contrary, neither  $k_{\text{PSS}}$  nor  $k_{\text{PWG}}$  share this property, and require recomputations for each hyperparameter choice. Note however that this improvement may no longer hold if one uses other methods to tune parameters. For instance, using  $k_{\text{PWG}}$  without cross-validation is possible with the heuristics given by the authors in [19], and leads to smaller training times, but also to worse accuracies.

#### 4.1 3D shape segmentation

Our first task, whose goal is to produce point classifiers for 3D shapes, follows that presented in [6].

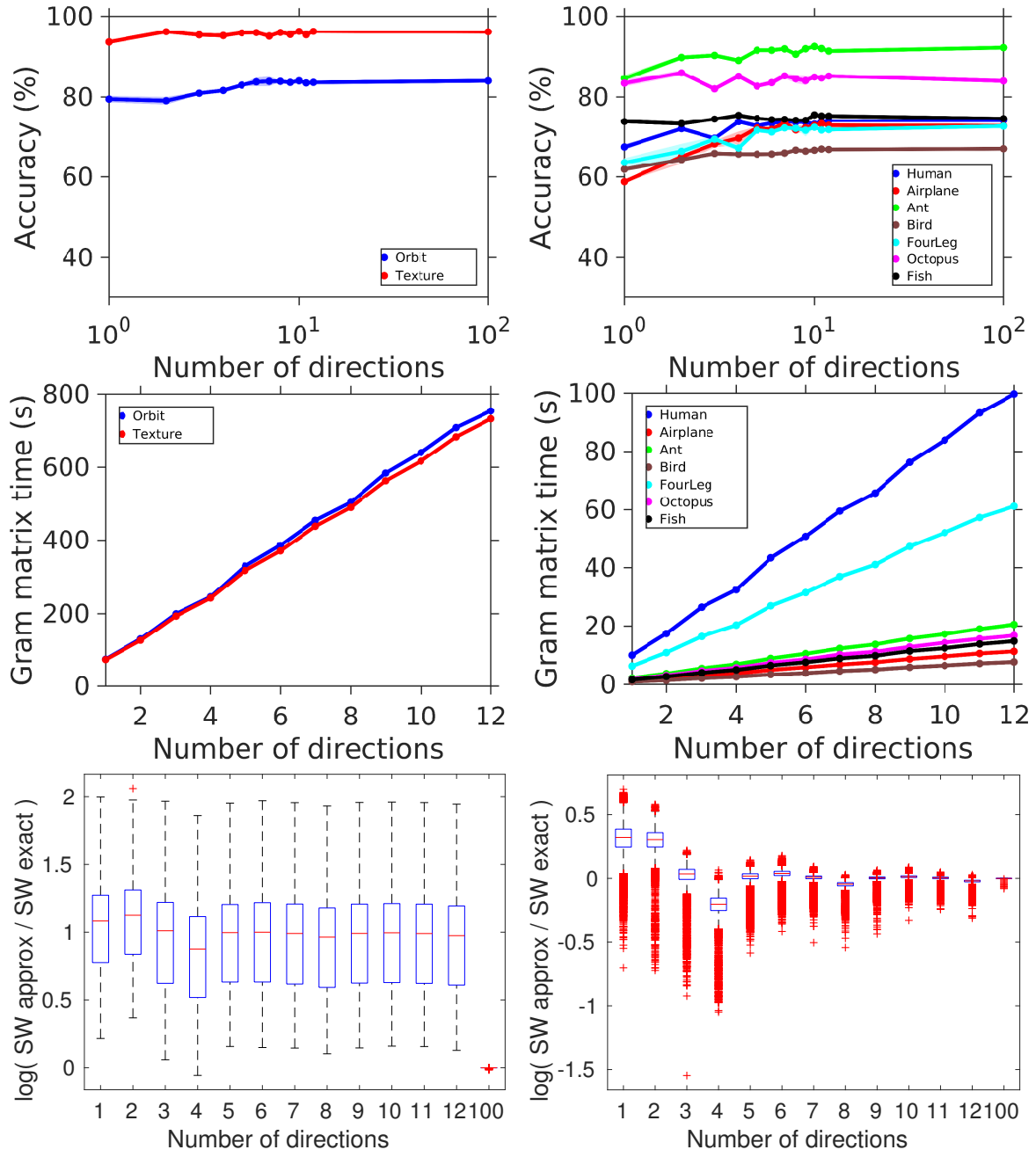


Figure 5: The first column corresponds to the orbit recognition and the texture classification while the second column corresponds to 3D shape segmentation. On each column, the first row shows the dependence of the accuracy on the number of directions, the second row shows the dependence of a single Gram matrix computation time, and the third row shows the dependence of the ratio of the approximation of SW and the exact SW. Since the box plot of the ratio for orbit recognition is very similar to that of 3D shape segmentation, we only give the box plot of texture classification in the first column.

**Data.** We use some categories of the mesh segmentation benchmark of Chen et al. [12], which contains 3D shapes classified in several categories (“airplane”, “human”, “ant”...). For each category, our goal is to design a classifier that can assign, to each point in the shape, a label that describes the relative location of that point in the shape. For instance, possible labels are, for the human category, “head”, “torso”, “arm”... To train classifiers, we compute a PD per point using the geodesic distance function to this point—see [6] for details. We use 1-dimensional persistent homology (0-dimensional would not be informative since the shapes are connected, leading to solely one point with coordinates  $(0, +\infty)$  per PD). For each category, the training set contains one hundredth of the points of the first five 3D shapes, and the test set contains one hundredth of the points of the remaining shapes in that category. Points in training and test sets are evenly sampled. See Figure 4. Here, we focus on comparison between PDs, and not on achieving state-of-the-art results. It has been proven that PDs bring complementary information to classical descriptors in this task—see [6], hence reinforcing their discriminative power with appropriate kernels is of great interest. Finally, since data points are in  $\mathbb{R}^3$ , we set the  $p$  parameter of  $k_{\text{PWG}}$  to 5.

**Results.** Classification accuracies are given in Table 2. For most categories,  $k_{\text{SW}}$  outperforms competing kernels by a significant margin. The variance of the results over the run is also less than that of its competitors. However, training times are not better in general. Hence, we also provide the results for an approximation of  $k_{\text{SW}}$  with 10 directions. As one can see from Table 2 and from Figure 5, this approximation leaves the accuracies almost unchanged, while the training times become comparable with the ones of the other competitors. Moreover, according to Figure 5, using even less directions would slightly decrease the accuracies, but still outperform the competitors performances, while decreasing even more the training times.

## 4.2 Orbit recognition

In our second experiment, we use synthetized data. The goal is to retrieve parameters of dynamical system orbits, following an experiment proposed in [1].

**Data.** We study the *linked twist map*, a discrete dynamical system modeling fluid flow. It was used in [17] to model flows in DNA microarrays. Its orbits can be computed given a parameter  $r > 0$  and initial positions  $(x_0, y_0) \in [0, 1] \times [0, 1]$  as follows:

$$\begin{cases} x_{n+1} = x_n + ry_n(1 - y_n) \mod 1 \\ y_{n+1} = y_n + rx_{n+1}(1 - x_{n+1}) \mod 1 \end{cases}$$

Depending on the values of  $r$ , the orbits may exhibit very different behaviors. For instance, as one can see in Figure 3, when  $r$  is 3.5, there seems to be no interesting topological features in the orbit, while voids form for  $r$  parameters around 4.3. Following [1], we use 5 different parameters  $r = 2.5, 3.5, 4, 4.1, 4.3$ , that act as labels. For each parameter, we generate 100 orbits with 1000 points and random initial positions. We then compute the PDs of the distance functions to the point clouds with the GUDHI library [33] and we use them (in all homological dimensions) to produce an orbit classifier that predicts the parameter values, by training over a 70%-30% training-test split of the data. Since data points are in  $\mathbb{R}^2$ , we set the  $p$  parameter of  $k_{\text{PWG}}$  to 4.

**Results.** Since the PDs contain thousands of points, we use kernel approximations to speed up the computation of the Gram matrices. In order for the approximation error to be bounded by  $10^{-3}$ , we use an approximation of  $k_{\text{SW}}$  with 6 directions (as one can see from Figure 5, this has a small impact on the accuracy), we approximate  $k_{\text{PWG}}$  with 1000 random Fourier features [27], and we approximate  $k_{\text{PSS}}$  using Fast Gauss Transform [23] with a normalized error of  $10^{-10}$ . One can see from Table 2 that the accuracy is increased a lot with  $k_{\text{SW}}$ . Concerning training times, there is also a large improvement since we tune the parameters with grid search. Indeed, each Gram matrix needs not be recomputed for each parameter when using  $k_{\text{SW}}$ .

### 4.3 Texture classification

Our last experiment is inspired from [29] and [22]. We use the *OUTEX00000* data base [24] for texture classification.

**Data.** PDs are obtained for each texture image by computing first the sign component of CLBP descriptors [16] with radius  $R = 1$  and  $P = 8$  neighbors for each image, and then compute the persistent homology of this descriptor using the GUDHI library [33]. See Figure 4. Note that, contrary to the experiment of [29], we do not downsample the images to  $32 \times 32$  images, but keep the original  $128 \times 128$  images. Following [29], we restrict the focus to 0-dimensional persistent homology. We also use the first 50%-50% training-test split given in the database to produce classifiers. Since data points are in  $\mathbb{R}^2$ , we set the  $p$  parameter of  $k_{\text{PWG}}$  to 4.

**Results** We use the same approximation procedure as in Section 4.2. According to Figure 5, even though the approximation of SW is rough, this has again a small impact on the accuracy, while reducing the training time by a significant margin. As one can see from Table 2, using  $k_{\text{PSS}}$  leads to almost state-of-the-art results [24, 16], closely followed by the accuracies of  $k_{\text{SW}}$  and  $k_{\text{PWG}}$ . The best timing is given by  $k_{\text{SW}}$ , again because we use grid search. Hence,  $k_{\text{SW}}$  almost achieves the best result, and its training time is better than the ones of its competitors, due to the grid search parameter tuning.

### 4.4 Metric Distortion.

To illustrate the equivalence theorem, we also show in Figure 6 a scatter plot where each point represents the comparison of two PDs taken from the Airplane segmentation data set. Similar plots can be obtained with the other datasets considered here. For all points, the x-axis quantifies the first diagram distance  $d_1$  for that pair, while the y-axis is the logarithm of the RKHS distance induced by either  $k_{\text{SW}}$ ,  $k_{\text{PSS}}$ ,  $k_{\text{PWG}}$  or a Gaussian kernel directly applied to  $d_1$ , to obtain comparable quantities. We use the parameters given by the cross-validation procedure described above. One can see that the distances induced by  $k_{\text{SW}}$  are less spread than the others, suggesting that the metric induced by  $k_{\text{SW}}$  is more discriminative. Moreover the distances given by  $k_{\text{SW}}$  and the Gaussian kernel on  $d_1$  exhibit the same behavior, suggesting that  $k_{\text{SW}}$  is the best natural equivalent of a Gaussian kernel for PDs.

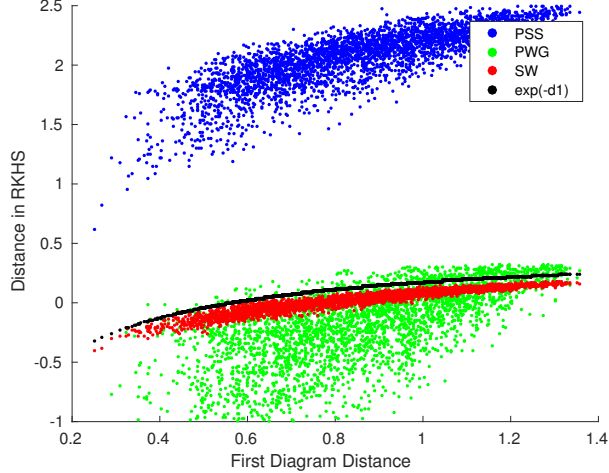


Figure 6: We show how the metric  $d_1$  is distorted. Each point represents a pair of PDs and its abscissae is the first diagram distance between them. Depending on the point color, its ordinate is the logarithm of the distance between PDs in the RKHS induced by either  $k_{\text{PSS}}$  (blue points),  $k_{\text{PWG}}$  (green points),  $k_{\text{SW}}$  (red points) and a Gaussian kernel on  $d_1$  (black points).

## 5 Conclusion

In this article, we introduce the *Sliced Wasserstein kernel*, a new kernel for PDs that is provably *equivalent* to the first diagram distance between PDs. We provide fast algorithms to approximate it, and show on several datasets substantial improvements in accuracy and training times (when tuning parameters is done with grid search) over competing kernels. A particularly appealing property of that kernel is that it is infinitely divisible, substantially facilitating the tuning of parameters through cross validation.

**Acknowledgements.** SO was supported by ERC grant Gudhi and by ANR project TopData. MC was supported by a *chaire de l'INDEX Paris Saclay*.

## References

- [1] Henry Adams, Tegan Emerson, Michael Kirby, Rachel Neville, Chris Peterson, Patrick Shipman, Sofya Chepushtanova, Eric Hanson, Francis Motta, and Lori Ziegelmeier. Persistence Images: A Stable Vector Representation of Persistent Homology. *Journal of Machine Learning Research*, 18(8):1–35, 2017.
- [2] Ulrich Bauer and Michael Lesnick. Induced matchings and the algebraic stability of persistence barcodes. *Journal of Computational Geometry*, 6(2):162–191, 2015.
- [3] Christian Berg, Jens Christensen, and Paul Ressel. *Harmonic Analysis on Semigroups: Theory of Positive Definite and Related Functions*. Springer, 1984.
- [4] Peter Bubenik. Statistical Topological Data Analysis using Persistence Landscapes. *Journal of Machine Learning Research*, 16:77–102, 2015.

[5] Gunnar Carlsson, Vin de Silva, and Dmitriy Morozov. Zigzag Persistent Homology and Real-valued Functions. In *Proceedings of the 25th Symposium on Computational Geometry*, pages 247–256, 2009.

[6] Mathieu Carrière, Steve Oudot, and Maks Ovsjanikov. Stable Topological Signatures for Points on 3D Shapes. *Computer Graphics Forum*, 34, 2015.

[7] C. Chang and C. Lin. LIBSVM: A library for support vector machines. *ACM Transactions on Intelligent Systems and Technology*, 2:1–27, 2011. Software available at <http://www.csie.ntu.edu.tw/~cjlin/libsvm>.

[8] Frédéric Chazal, David Cohen-Steiner, Marc Glisse, Leonidas Guibas, and Steve Oudot. Proximity of Persistence Modules and their Diagrams. In *Proceedings of the 25th Symposium on Computational Geometry*, pages 237–246, 2009.

[9] Frédéric Chazal, David Cohen-Steiner, Leonidas Guibas, Facundo Mémoli, and Steve Oudot. Gromov-Hausdorff Stable Signatures for Shapes using Persistence. *Computer Graphics Forum*, pages 1393–1403, 2009.

[10] Frédéric Chazal, Vin de Silva, Marc Glisse, and Steve Oudot. *The Structure and Stability of Persistence Modules*. Springer, 2016.

[11] Frédéric Chazal, Vin de Silva, and Steve Oudot. Persistence stability for geometric complexes. *Geometriae Dedicata*, pages 1–22, 2013.

[12] X. Chen, A. Golovinskiy, and T. Funkhouser. A Benchmark for 3D Mesh Segmentation. *ACM Transactions on Graphics*, 28(3):1–12, 2009.

[13] David Cohen-Steiner, Herbert Edelsbrunner, and John Harer. Stability of Persistence Diagrams. *Discrete and Computational Geometry*, 37(1):103–120, 2007.

[14] Barbara di Fabio and Massimo Ferri. Comparing persistence diagrams through complex vectors. *CoRR*, abs/1505.01335, 2015.

[15] Herbert Edelsbrunner and John Harer. *Computational Topology: an introduction*. AMS Bookstore, 2010.

[16] Zhenhua Guo, Lei Zhang, and David Zhang. A completed modeling of local binary pattern operator for texture classification. *IEEE Transaction on Image Processing*, pages 1657–1663, 2010.

[17] Jan-Martin Hertzsch, Rob Sturman, and Stephen Wiggins. DNA microarrays: design principles for maximizing ergodic, chaotic mixing. In *Small*, volume 3, pages 202–218, 2007.

[18] Yasuaki Hiraoka, Takenobu Nakamura, Akihiko Hirata, Emerson Escolar, Kaname Matsue, and Yasumasa Nishiura. Hierarchical structures of amorphous solids characterized by persistent homology. In *Proceedings of the National Academy of Science*, volume 26, 2016.

[19] Genki Kusano, Kenji Fukumizu, and Yasuaki Hiraoka. Persistence Weighted Gaussian Kernel for Topological Data Analysis. In *Proceedings of the 33rd International Conference on Machine Learning*, pages 2004–2013, 2016.

- [20] Genki Kusano, Kenji Fukumizu, and Yasuaki Hiraoka. Kernel method for persistence diagrams via kernel embedding and weight factor. *CoRR*, abs/1706.03472, 2017.
- [21] Roland Kwitt, Stefan Huber, Marc Niethammer, Weili Lin, and Ulrich Bauer. Statistical Topological Data Analysis - A Kernel Perspective. In *Advances in Neural Information Processing Systems 28*, pages 3070–3078, 2015.
- [22] Chunyuan Li, Maks Ovsjanikov, and Frédéric Chazal. Persistence-Based Structural Recognition. In *IEEE Conference on Computer Vision and Pattern Recognition*, pages 2003–2010, 2014.
- [23] Vlad Morariu, Balaji Srinivasan, Vikas Raykar, Ramani Duraiswami, and Larry Davis. Automatic online tuning for fast Gaussian summation. In *Advances in Neural Information Processing Systems 21*, pages 1113–1120, 2009.
- [24] Timo Ojala, Topi Mäenpää, Matti Pietikäinen, Jaakko Viertola, Juha Kyllonen, and Sami Huovinen. Outex - new framework for empirical evaluation of texture analysis algorithms. In *Proceedings of the 16th International Conference on Pattern Recognition*, pages 701–706, 2002.
- [25] Steve Oudot. *Persistence Theory: From Quiver Representations to Data Analysis*. Number 209 in Mathematical Surveys and Monographs. American Mathematical Society, 2015.
- [26] Julien Rabin, Gabriel Peyré, Julie Delon, and Marc Bernot. Wasserstein barycenter and its application to texture mixing. In *International Conference on Scale Space and Variational Methods in Computer Vision*, pages 435–446, 2011.
- [27] Ali Rahimi and Benjamin Recht. Random Features for Large-Scale Kernel Machines. In *Advances in Neural Information Processing Systems 20*, pages 1177–1184, 2008.
- [28] Jan Reininghaus, Stefan Huber, Ulrich Bauer, and Roland Kwitt. A Stable Multi-Scale Kernel for Topological Machine Learning. *CoRR*, abs/1412.6821, 2014.
- [29] Jan Reininghaus, Stefan Huber, Ulrich Bauer, and Roland Kwitt. A Stable Multi-Scale Kernel for Topological Machine Learning. In *IEEE Conference on Computer Vision and Pattern Recognition*, 2015.
- [30] Vanessa Robins and Katharine Turner. Principal Component Analysis of Persistent Homology Rank Functions with case studies of Spatial Point Patterns, Sphere Packing and Colloids. *Physica D: Nonlinear Phenomena*, 334:1–186, 2016.
- [31] Filippo Santambrogio. *Optimal transport for applied mathematicians*. Springer, 2015.
- [32] Gurjeet Singh, Facundo Mémoli, Tigran Ishkhanov, Guillermo Sapiro, Gunnar Carlsson, and Dario Ringach. Topological analysis of population activity in visual cortex. *Journal of Vision*, 8, 2008.
- [33] The GUDHI Project. *GUDHI User and Reference Manual*. GUDHI Editorial Board, 2015.
- [34] Cédric Villani. *Optimal transport : old and new*. Springer, 2009.